Charge-density-wave instabilities expected in monophosphate tungsten bronzes

Enric Canadell
Laboratoire de Chimie Théorique, Université de Paris–Sud, 91405 Orsay, France

Myung-Hwan Whangbo
Department of Chemistry, North Carolina State University, Raleigh, North Carolina 27695-8204
(Received 16 July 1990)

On the basis of tight-binding band calculations, we examined the electronic structures of the tungsten oxide layers found in the monophosphate tungsten bronze (MPTB) phases. The Fermi surfaces of these MPTB phases consist of five well-nested one- and two-dimensional pieces. We calculated the nesting vectors of these Fermi surfaces and discussed the expected charge-density-wave instabilities.

I. INTRODUCTION

The essential structural building blocks of the monophosphate tungsten bronzes (MPTB), $(PO_2)_4(WO_3)_p(WO_3)_q$ (p,q being integers), are the perovskite-type layers made up of WO_6 octahedra.[1,2] These tungsten oxide (W-O) layers are linked by PO_4 tetrahedra. Depending upon how the PO_4 tetrahedra link the W-O layers, the MPTB phases have either pentagonal or hexagonal tunnels between their W-O layers (and hence called the $MPTB_p$ and $MPTB_h$ phases, respectively). The $MPTB_h$ phases are found with alkali-metal atoms Na or K in their hexagonal channels,[2] so that their formulas are given by $A_x(PO_2)_4(WO_3)_p(WO_3)_q$. In the absence of alkali-metal atoms, the MPTB phases possess the pentagonal tunnels,[1] and thus the $MPTB_p$ phases have the formulas $(PO_2)_4(WO_3)(WO_3)_q$.

The Magnéli phases γ- and η-Mo_4O_{11} contain the perovskite-type layers made up of MoO_6 octahedra,[3] which are isostructural with the perovskite-type W-O layers of the MPTB phases, and these Mo-O layers are linked by MoO_4 tetrahedra. With the notation designed for the MPTB phases, the Magnéli phase Mo_4O_{11} is written as $(MoO_2)_4(MoO_3)_6(MoO_3)_6$, which is equivalent to $(Mo_4O_{11})_4$. Therefore, the crystal structures of γ- and η-Mo_4O_{11} are very similar to those of the $MPTB_p$ and $MPTB_h$ phases, i.e., $(PO_2)_4(WO_3)_6(WO_3)_6$ and $A_x(PO_2)_4(WO_3)_6(WO_3)_6$, respectively. The Magnéli phases γ- and η-Mo_4O_{11} exhibit resistivity anomalies resulting from a charge-density wave[4] (CDW) associated with the partially filled t_{2g}-block bands of their perovskite-type Mo-O layers.[5] Since the W-O layers of the MPTB phases are isostructural with the Mo-O layers of the Magnéli phases and since the W and Mo atoms are in the same family of the Periodic Table, the MPTB phases are expected to exhibit CDW instabilities. The formal oxidation state of P in the PO_4 tetrahedra of the MPTB phases is $+5$, while that of Mo in the MoO_4 tetrahedra of the Magnéli phases is $+6$. Consequently, the Mo-O layers of the Magnéli phase have more d electrons than do the W-O layers of the corresponding MPTB phase, so that the electronic instabilities of the Mo-O and W-O layers are expected to differ somewhat.

Recently, the $MPTB_p$ phase $(PO_2)_4(WO_3)_p(WO_3)_6$ has been found[6] to have resistivity anomalies which resemble those of $NbSe_3$, a well-established CDW material.[7] The band electronic structure study of $(PO_2)_4(WO_3)_6(WO_3)_6$ shows[6] that it has well-nested one-dimensional (1D) and two-dimensional (2D) Fermi surfaces. Thus the resistivity anomalies of $(PO_2)_4(WO_3)_6(WO_3)_6$ are suggested to originate from the CDW instabilities associated with the Fermi surface nesting.[6] Recently, we have examined[8] the band electronic structures of a series of MPTB phases which reveals that all these MPTB phases possess 1D and 2D metallic bands as in the case of the Magnéli phases γ- and η-Mo_4O_{11} and the $MPTB_p$ phase $(PO_2)_4(WO_3)_6(WO_3)_6$.

In the present study, we examine the Fermi surfaces of all MPTB phases with known crystal structure. Our objective is to probe how the Fermi surface topologies vary as a function of the number of d electrons per unit cell and the thickness of the perovskite-type W-O layers. The CDW vectors we calculate for the various MPTB phases should be verifiable experimentally by diffuse x-ray scattering and neutron-diffraction measurements.

II. CRYSTAL STRUCTURE

The indices p and q used in the formulas $(PO_2)_4(WO_3)_p(WO_3)_q$ or $A_x(PO_2)_4(WO_3)_p(WO_3)_q$ refer to the number of WO_6 octahedra (per unit cell) needed to form the W-O layers. In most cases, p and q are identical so that one obtains alternative formulas $(PO_2)_4(WO_3)_{2m}$ and $A_x(PO_2)_4(WO_3)_{2m}$ (m being an integer). In certain cases, however, the indices p and q are different as in $(PO_2)_4(WO_3)_4(WO_3)_6$.

Let us now describe the structural patterns of the perovskite-type W-O layers by considering the W-O layer with $p=4$ as an example. The W_4O_{21} unit of Fig. 1(a) is constructed from four WO_6 octahedra by sharing the equatorial corners, and the W_4O_{18} chain of Fig. 1(b) is ob-

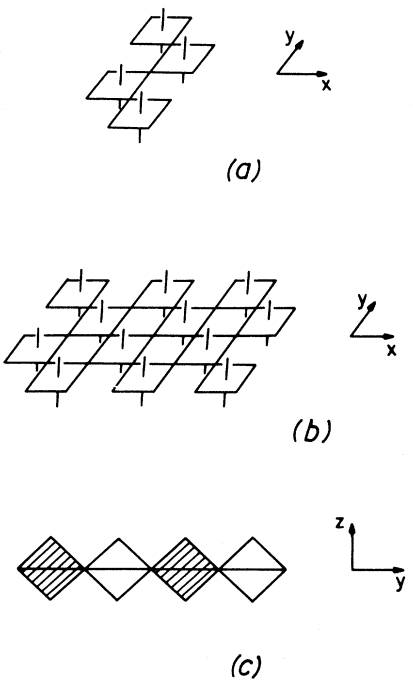

FIG. 1. (a) Perspective view of the W_4O_{21} unit, (b) perspective view of the W_4O_{18} chain, and (c) projection view of the W_4O_{18} chain.

tained by condensing the W_4O_{21} units. For simplicity, the W_4O_{18} chain of Fig. 1(b) can be represented by the projection view shown in Fig. 1(c) along the chain direction. The W_4O_{18} chains of Fig. 1(c) can be condensed to form the W_4O_{16} layers of Fig. 2(a) by sharing their axial oxygen atoms. In the W_4O_{16} layer, the first octahedron

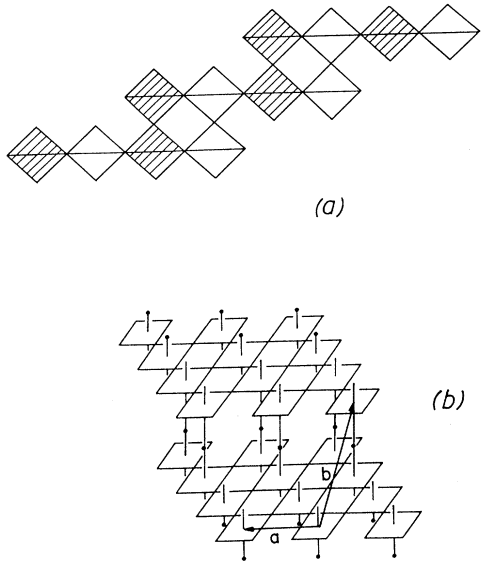

FIG. 2. (a) Projection view of the W_4O_{16} layer and (b) perspective view of the W_4O_{16} layer.

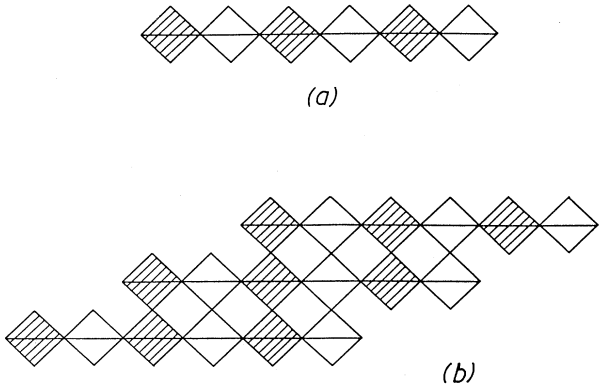

FIG. 3. (a) Projection view of the W_6O_{26} chain and (b) projection view of the W_6O_{22} step layer.

of one W_4O_{18} chain shares its axial oxygen atom with the third octahedron of the adjacent W_4O_{18} chain [i.e., (13)-condensation]. Shown in Fig. 2(b) is a perspective view of the W_4O_{16} layer which is a step layer with each W_4O_{18} chain as a step. In a similar manner, one can condense the W_6O_{26} chains [Fig. 3(a)] to form the W_6O_{22} step layer Fig. 3(b) by (13)-condensation. Figure 4 shows projection views of the three-dimensional (3D) lattices of several representative MPTB phases, where solid triangles represent PO_4 tetrahedra.

III. COMPUTATIONAL METHOD

The band electronic structures of the MPTB phases presented in our work are obtained by performing tight-binding band calculations[9] based upon the extended Hückel method.[10] In the tight-binding method, the electronic structure of a crystalline solid is described by constructing band orbitals as a linear combination of atomic orbitals. With a set of Slater type atomic orbitals χ_i, the

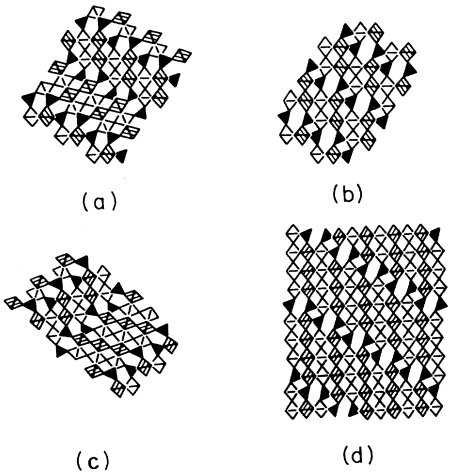

FIG. 4. Projection views of the MPTB phases: (a) $(PO_2)_4(WO_3)_4(WO_3)_4$, (b) $Na_x(PO_2)_4(WO_3)_4(WO_3)_4$, (c) $(PO_2)_4(WO_3)_4(WO_3)_6$, and (d) $Na_x(PO_2)_4(WO_3)_7(WO_3)_7$.

extended Hückel Hamiltonian H^{eff} is specified by defining its off-diagonal matrix elements $H_{ij}=\langle\chi_i|H^{eff}|\chi_j\rangle$ as

$$H_{ij}=KS_{ij}(H_{ii}+H_{jj})/2\ . \quad (1)$$

In this Wolfsberg-Helmholz approximation,[11] S_{ij} is the overlap integral $\langle\chi_i|\chi_j\rangle$ between the orbitals χ_i and χ_j, K is a constant (i.e., 1.75), and the diagonal elements $H_{ii}=\langle\chi_i|H^{eff}|\chi_i\rangle$ and $H_{jj}=\langle\chi_j|H^{eff}|\chi_j\rangle$ are the valence shell ionization potentials (VSIP) of the orbitals χ_i and χ_j, respectively. The VSIP values are treated as empirical parameters like the exponents of the Slater-type orbitals. Details of the atomic parameters employed in the present work are taken from our previous studies.[8,12] In the present study, we employ the modified Wolfsberg-Helmholz approximation,[13] in which the constant K of Eq. (1) is repaced with another constant $K'=K+\Delta^2+\Delta^4(1-K)$, where $\Delta=(H_{ii}-H_{jj})/(H_{ii}+H_{jj})$.

Over the past decade, the extended Hückel tight-binding (EHTB) method has been successfully applied to investigate the electronic structures of numerous low-dimensional inorganic solids containing transition-metal elements. The EHTB calculations on the CDW materials such as niobium and tantalum chalcogenides[7(c),14] and molybdenum oxides[5,15] are in excellent agreement with the experiment.

IV. BAND ELECTRONIC STRUCTURE OF THE IDEAL W-O LAYER

Our previous study[8] showed that the band electronic structures of various MPTB phases are very similar, and their characteristic features are also exhibited by an ideal W-O layer made up of regular WO_6 octahedra. Thus in this section we describe their essential features on the basis of the band electronic structure calculated for the ideal W_4O_{16} step layer of Fig. 2 which we construct from regular WO_6 octahedra (with the average W-O distance of 1.916 Å).

Figure 5 shows the dispersion of the t_{2g}-block bands calculated for the ideal W_4O_{16} step layer, where $\Gamma=(0,0)$, $X=(a^*/2,0)$, $Y=(0,b^*/2)$, and $M=(a^*/2,b^*/2)$. In order to discuss the Fermi surfaces associated with these bands, we consider the electron counting appropriate for the MPTB phases $(PO_2)_4(WO_3)_m(WO_3)_m$, where m is the number of W atoms per unit cell in each W-O layer. With the typical oxidation scheme of P^{5+} and O^{2-}, the average oxidation state of W in $(PO_2)_4(WO_3)_m(WO_3)_m$ is given by $(6m-2)/m$. Consequently, each step layer has two d electrons per unit cell [i.e., $6m-m(6m-2)/m=2$], regardless of the m value. For $A_x(PO_2)_4(WO_3)_m(WO_3)_m$, the oxidation state of the alkali metal is $+1$, so that each step layer has $2+x/2$ electrons per unit cell to fill its t_{2g}-block bands. The dashed lines of Fig. 5 refer to the Fermi level for cases when the number of d electrons per unit cell (i.e., N) is two, three, or four. The $N=2$ case is appropriate for the $MPTB_p$ phases. The $N=4$ case is appropriate for the Magnéli phases γ and η-Mo_4O_{11} because, as already noted, their formulas are equivalent to $(MoO_2)_4(MoO_3)_6(MoO_3)_6$ and because the Mo oxidation state in the MoO_4 tetrahedra is $+6$ instead of $+5$ found for the P atom in the PO_4 tetrahedra of the MPTB phases.[5] Note that, for all three case of $N=2$, 3, and 4, only the bottom three bands of Fig. 5 become partially filled (labeled a and b). Band a is 1D is nature, while band b consists of two subbands and have 2D character. The orbital nature of these bands has been analyzed in detail elsewhere.[5]

The electron and hole Fermi surfaces of the three par-

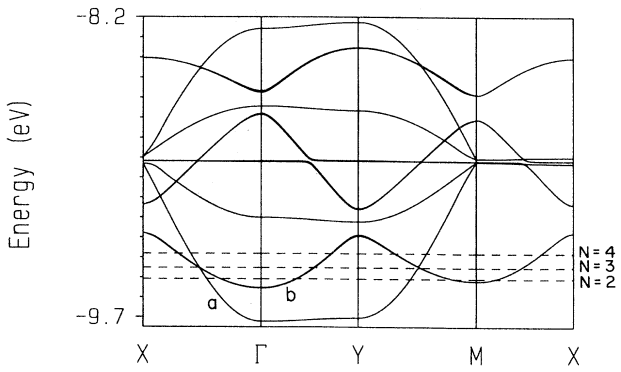

FIG. 5. Dispersion relations of the t_{2g}-block bands calculated for the ideal W_4O_{16} layer (Fig. 2), where the dashed line refers to the Fermi level for $N=2$, 3, and 4.

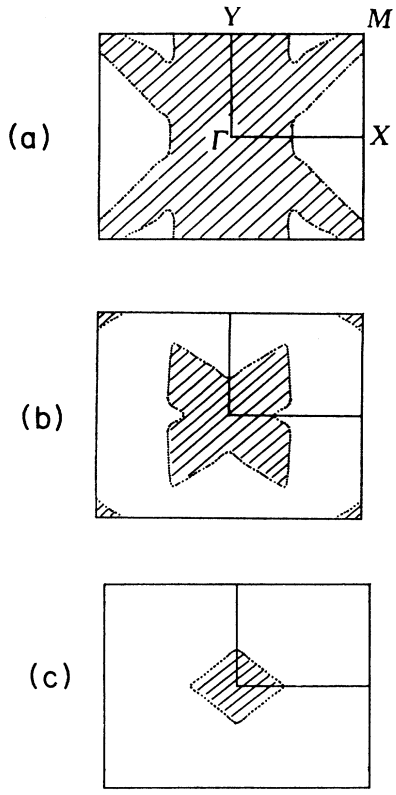

FIG. 6. Fermi surfaces associated with the partially filled bands of Fig. 5 for $N=2$, where the filled regions of wave vectors are shown by shading.

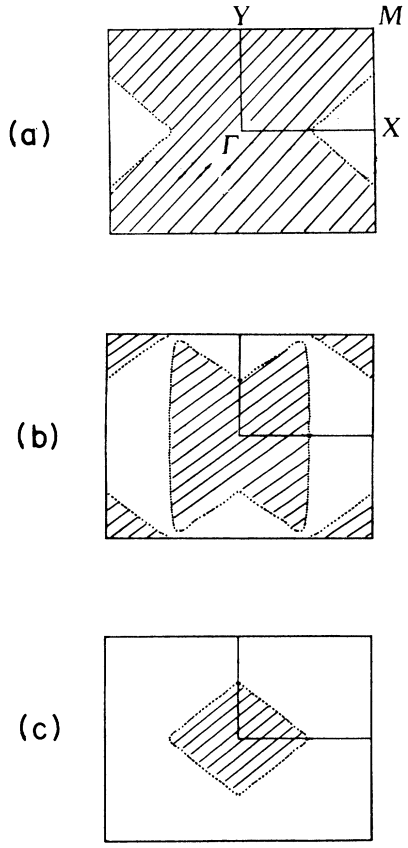

FIG. 7. Fermi surfaces associated with the partially filled bands of Fig. 5 for $N=3$, where the filled regions of wave vectors are shown by shading.

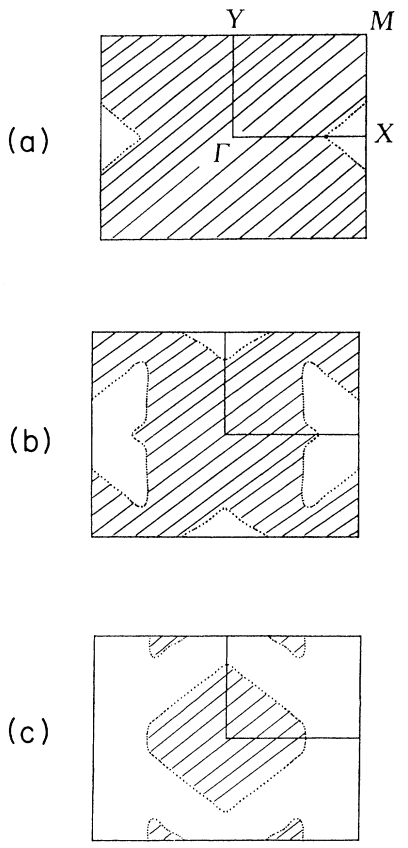

FIG. 8. Fermi surfaces associated with the partially filled bands of Fig. 5 for $N=4$, where the filled regions of wave vectors are shown by shading.

tially filled bands calculated for the cases of $N=2$, 3, and 4 are shown in Figs. 6, 7, and 8, respectively. We combine the hole and electron Fermi surfaces of Fig. 6 in Fig. 9(a), those of Fig. 7 in Fig. 9(a), and those of Fig. 8 in Fig. 9(c). The combined Fermi surfaces of Fig. 9(a) originate from the 1D surface associated with the 1D band a [Fig. 10(a)] and the two 2D surfaces associated with the 2D bands b [Figs. 10(a) and 10(c)]. These features are also present in the combined Fermi surfaces of Figs. 9(b) and 9(c). The Fermi surface of Fig. 10(b) consists of rhombuses centered at Γ and M, while that of Fig. 10(c) consists of rhombuses centered at X and Y. We now examine why these rhombus-shaped Fermi surfaces arise from the 2D band b of Fig. 5. Figures 11(a) and 11(b) show dispersion relations of the t_{2g}-block bands along $\Gamma \rightarrow P \rightarrow M$ and $X \rightarrow P \rightarrow Y$. Here the wave vector P is the crossing point of the $\Gamma \rightarrow M$ and $X \rightarrow Y$ lines in the first Brillouin zone (Fig. 12). Band b consists of two subbands. Along $\Gamma \rightarrow P \rightarrow M$ [Fig. 11(a)], the lower subband is nearly flat but the upper subband is dispersive with a maximum at P. At Γ and M, the two subbands are degenerate. Along $X \rightarrow P \rightarrow Y$ [Fig. 11(b)], however, the lower subband is dispersive with a minimum at P but the upper subband is nearly flat. At X and Y, the two subbands are degenerate. The two subbands have a lower energy at Γ and M than at X and Y. Consequently, along $\Gamma \rightarrow P \rightarrow M$, the upper subband is cut twice by the Fermi level nearly symmetrically around P, while along $X \rightarrow P \rightarrow Y$ the lower subband is cut twice by the Fermi level nearly symmetrically around P. This topology of the dispersion relations of the two subbands is responsible for the rhombus-shaped 2D Fermi surfaces centered at Γ and M in Fig. 10(b) and those at X and Y in Fig. 10(c). A detailed analysis of the orbital nature of the two subbands along $\Gamma \rightarrow P \rightarrow M$ and $X \rightarrow P \rightarrow Y$ is given elsewhere.[16]

The 1D Fermi surface of Fig. 10(a) has the nesting vector q_{1D} as shown in Fig. 13(a). The rhombus-shaped 2D Fermi surfaces centered at Γ, M, X, and Y in Figs. 10(b) and 10(c) have the nesting vectors q_Γ, q_M, q_X, and q_Y, respectively, as shown in Fig. 13(b). If the sides of the rhombuses centered at Γ and M are parallel to the corresponding sides of the rhombuses at X and Y, one obtains a single nesting vector q_{2D} or q'_{2D} (instead of q_Γ, q_M, q_X and q_Y) as shown in Figs. 14(a) and 14(b). Inspection of Figs. 9(a)–9(c) shows that the rhombuses are nearly parallel only when the N value (i.e., the number of d electrons per unit cell) is close to 4 [i.e., Fig. 9(c)]. The Mo-O step layers of the Magnéli phases γ- and η-Mo_4O_{11} corre-

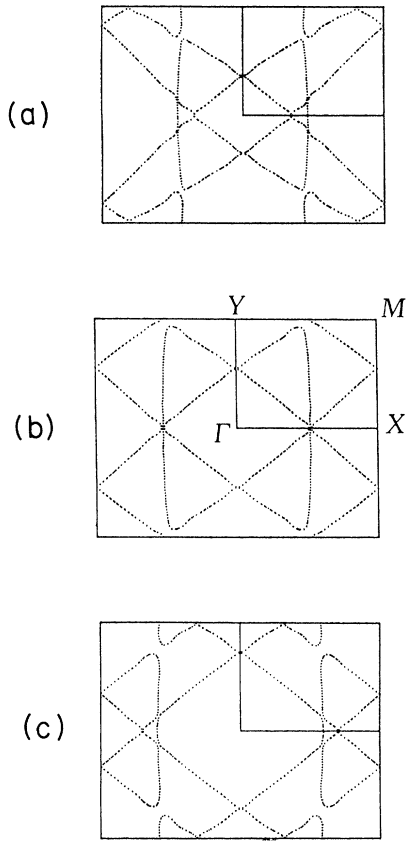

FIG. 9. Combined Fermi surfaces of Figs. 6, 7, and 8 in (a), (b), and (c), respectively.

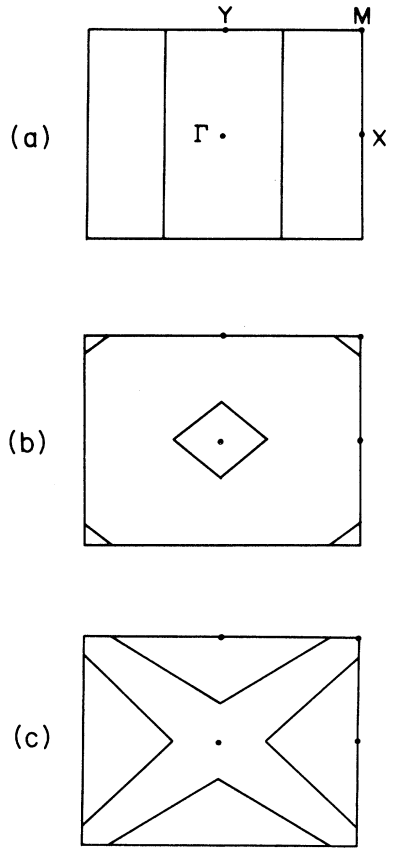

FIG. 10. 1D and 2D Fermi surfaces leading to the combined Fermi surfaces of Fig. 9(a); (a) 1D Fermi surface, (b) 2D Fermi surfaces centered at Γ and M, and (c) 2D Fermi surfaces centered at X and Y. The rhombus-shaped 2D Fermi surfaces centered at X, Y, and M can be readily constructed by repeating the patterns of (b) and (c) in an extended zone scheme.

spond to this electron counting, and their Fermi surfaces are very close to those shown in Fig. 9(c).[5] Experimentally, γ- and η-Mo_4O_{11} are found to exhibit a CDW with nesting vector q_{2D}.[3–5]

V. CDW NESTING VECTORS OF REAL W-O LAYERS

Our EHTB calculations carried out for various W-O step layers of the $MPTB_p$ and $MPTB_h$ phases with known crystal structure show that their t_{2g}-block bands are qualitatively very similar to those of the ideal W_4O_{16}layer described in the previous section. The CDW nesting vectors q_i $(i=1D,\Gamma,M,X,Y)$ expected from the Fermi surfaces of these W-O step layers may be expressed as

$$q_i=\alpha\mathbf{a}^*\pm\beta\mathbf{b}^* \ , \tag{2}$$

where the reciprocal vectors $\mathbf{a}^*$ and $\mathbf{b}^*$ correspond to the intrastep and interstep repeat vectors $\mathbf{a}$ and $\mathbf{b}$ respectively [e.g., the vecors a and b, respectively, in the W_4O_{16} layer of Fig. 2(b)]. According to this description based upon the ideal W-O layers, the α values of q_Γ and q_X (or q_Y and q_M) or the β values of q_Γ and q_Y (or q_X and q_M) add up to be 0.5. The α and β values of the nesting vectors q_i

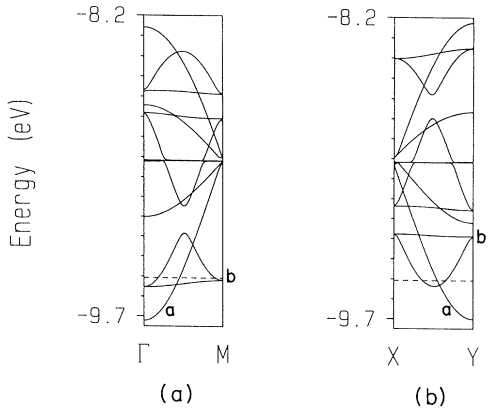

FIG. 11. Dispersion relations of the t_{2g}-block bands of the ideal W_4O_{16} layer (Fig. 2) along (a) $\Gamma\rightarrow P\rightarrow M$ and (b) $X\rightarrow P\rightarrow Y$. The dashed line refers to the Fermi level for $N=2$.

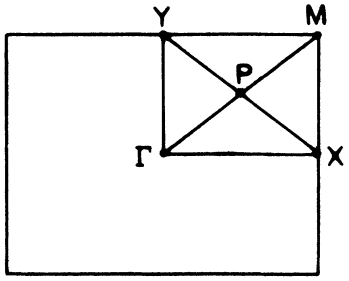

FIG. 12. First Brillouin zone for an ideal W_4O_{16} step layer (Fig. 2).

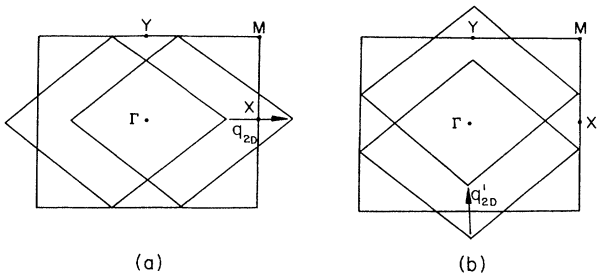

FIG. 14. Alternative CDW nesting vectors: (a) q_{2D} and (b) q'_{2D} constructed on the basis of Fig. 9(c).

($i=1D,\Gamma,M,X,Y$) calculated for the various W-O step layers studied in the present work are summarized in Table I.

Important points of Table I can be summarized as follows: (a) The "ideal" description of the CDW vectors given by Eq. (2) applies perfectly for the W_6O_{22} and W_7O_{25} layers. In general, the W_4O_{16} layers deviate slightly from the ideal description in that the α values of q_Γ and q_X (or q_Y and q_M) or the β values of q_Γ and q_Y (or q_X and q_M) do not exactly add up to be 0.5. (b) The departure from the ideal description is caused by the distortion of the W-O layer from the ideal structure made up of regular WO_6 octahedra. The extend of distortion in the W-O layers is generally larger for the thin W-O layer (e.g., W_4O_{16} layer) than for the thick W-O layer (e.g., W_6O_{22} or W_7O_{25} layer). (c) The sides of the Fermi surface rhombuses at Γ and M become more parallel to the corresponding sides of the Fermi surface rhombuses at X and Y as the N values becomes close to 4. This is also the case for the W_4O_{16} layers, although their structures are generally more distorted than those of the W_6O_{22} or the W_7O_{25} layers. Therefore, the q_{2D} and q'_{2D} vectors become relevant when $N\simeq 4$. The Fermi surfaces of the $MPTB_p$ and $MPTB_h$ phases calculated for $N=4$ show that $q_{2D}\simeq 0.25\mathbf{a}^*$, in good agreement with the experimental observation that $q_{2D}\simeq 0.23\mathbf{a}^*$ for γ- and η-Mo_4O_{11}.[5] The α and β values for the q_{2D} and q'_{2D} can be easily estimated from those of q_Γ, q_M, and q_X, and a_Y, and therefore are not listed in Table I.

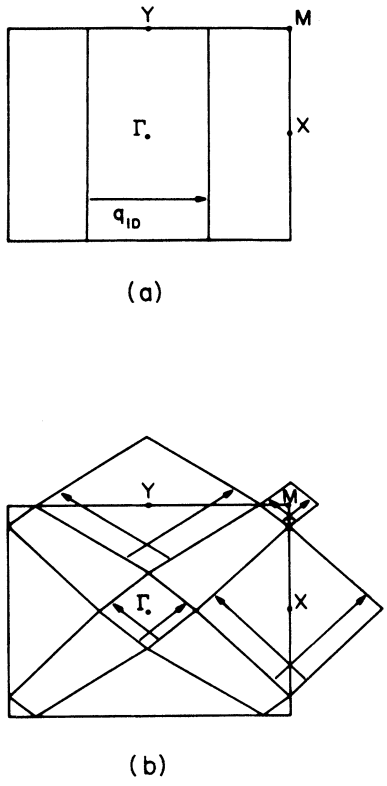

FIG. 13. CDW nesting vectors associated with the Fermi surfaces of Fig. 10: (a) q_{1D} and (b) q_Γ, q_M, and q_X, and q_Y.

VI. CONCLUDING REMARKS

The present EHTB calculations show that the MPTB phases have well-nested Fermi surfaces with nesting vectors q_{1D}, q_Γ, q_M, q_X, and q_Y. Thus these phases may in principle exhibit five different CDW instabilities when their W-O layers contain less than four d electrons per unit cell (e.g., $2<N<3$). When the value of N becomes close to 4, the four vector q_Γ, q_M, and q_X, and q_Y are expected to merge thereby leading to the alternative nesting vectors and q_{2D} and q'_{2D}. Energy lowering associated with a CDW formation increases as the area of the nested Fermi surface increases.[17] For the rhombus-shaped Fermi surfaces centered at Γ, M, X, and Y, the nested area increases with the size of the rhombus. Therefore, for the W-O steplayers with N value close to 2, CDW's resulting from q_X and q_Y are more likely to be observable than are those from q_Γ and q_M. To confirm the CDW nesting vectors predicted in the present work, diffuse x-ray scattering and/or neutron-diffraction measurements would be necessary. Our analysis[8] of the W-O layer band orbitals show that their partially filled bands are represented by the orbitals of all the WO_6 octahedra including those of the W-O layers surfaces. This situation differs considerably from that found for many Mo-O layers,[5,15(b),15(c)] in which the MoO_6 octahedra of the Mo-O layer surfaces

TABLE I. Components α and β of the CDW nesting vectors $\mathbf{q}_i = \alpha\mathbf{a}^* \pm \beta\mathbf{b}^*$ calculated for the various W-O step layers of the MPTB phases.

Compound	Step layer	N	i	α	β
$(PO_2)_4(WO_3)_4(WO_3)_4$[a]	W_4O_{16}	2	1D	0.41	0.00
			Γ	0.09	0.10
			M	0.09	0.10
			X	0.28	0.40
			Y	0.37	0.26
$(PO_2)_4(WO)_6(WO_3)_6$[b]	W_6O_{22}	2	1D	0.26	0.00
			Γ	0.21	0.22
			M	0.15	0.14
			X	0.29	0.36
			Y	0.35	0.28
$(PO_2)_4(WO_3)_4(WO_3)_6$[c]	W_4O_{16}	2	1D	0.38	0.00
			Γ	0.16	0.16
			M	0.08	0.10
			X	0.29	0.40
			Y	0.38	0.29
	W_6O_{22}	2	1D	0.30	0.00
			Γ	0.21	0.21
			M	0.14	0.13
			X	0.29	0.37
			Y	0.36	0.29
$K_x(PO_2)_4(WO_3)_4(WO_3)_4$[d] ($x=0.8$–$3.0$)	W_4O_{16}	2.40 ($x=0.8$)	1D	0.47	0.00
			Γ	0.09	0.09
			M	0.14	0.16
			X	0.24	0.34
			Y	0.30	0.23
		3.50 ($x=3.0$)	1D	0.50	0.00
			Γ	0.26	0.27
			M	0.29	0.29
			X	0.16	0.21
			Y	0.19	0.14
$Na_x(PO_2)_4(WO_3)_4(WO_3)_4$[e] ($x=1.1$–$1.5$)	W_4O_{16}	2.55 ($x=1.1$)	1D	0.43	0.00
			Γ	0.17	0.20
			M	0.18	0.19
			X	0.22	0.31
			Y	0.28	0.21
		2.75 ($x=1.5$)	1D	0.44	0.00
			Γ	0.20	0.21
			M	0.20	0.22
			X	0.22	0.28
			Y	0.30	0.20
$K_x(PO_2)_4(WO_3)_7(WO_3)_7$[f] ($x=1.4$–$1.7$)	W_7O_{25}	2.70 ($x=1.4$)	1D	0.36	0.00
			Γ	0.26	0.27
			M	0.23	0.23
			X	0.24	0.27
			Y	0.27	0.23
		2.85 ($x=1.7$)	1D	0.38	0.00
			Γ	0.28	0.29
			M	0.25	0.24
			X	0.22	0.26
			Y	0.25	0.21

TABLE I. (*Continued*).

Compound	Step layer	N	i	α	β
$Na_x(PO_2)_4(WO_3)_6(WO_3)_6$[g]	W_6O_{22}	2.80	1D	0.33	0.00
		($x=1.60$)	Γ	0.28	0.28
			M	0.26	0.24
			X	0.22	0.26
			Y	0.24	0.22
		4.0	1D	0.47	0.00
		($x=4.0$)	Γ	0.39	0.39
			M	0.37	0.37
			X	0.11	0.13
			Y	0.13	0.11

[a]Reference 1(a).
[b]Reference 1(b).
[c]Reference 1(c).
[d]Reference 2(a).
[e]Reference 2(b).
[f]References 2(c) and 2(d).
[g]Reference 2(b).

have practically no orbital contribution to their partially filled bands. Therefore, the CDW formation in the W-O layers of the $MPTB_h$ phases, $A_x(PO_2)_4(WO_3)_p(WO_3)_q$, can be prevented by the random potentials that cation disorder in the hexagonal channels may create, because the alkali-metal cations are close to the WO_6 octahedra of the W-O layer surfaces. In observing CDW phenomena of the MPTB phases, it would be more fruitful to investigate the $MPTB_p$ phases $(PO_2)_4(WO_3)_p(WO_3)_q$ rather than the $MPTB_h$ phases $A_x(PO_2)_4(WO_3)_p(WO_3)_q$. Our study strongly suggests that the MPTB phases should exhibit very rich CDW phenomena and therefore would be very exciting materials to study.

ACKNOWLEDGMENTS

This work was supported by the U.S. Department of Energy, Office of Basic Energy Sciences, Division of Materials Sciences under Grant De-FG05-86ER45259. We thank Dr. I. E.-I. Rachidi for some preliminary calculations at the initial stage of this work.

[1](a) J. P. Giroult, M. Goreaud, P. Labbé, and B. Raveau, Acta Crystallogr. Sect. B **37**, 2139 (1981); (b) P. Labbé, M. Goreaud, and B. Raveau, J. Solid State Chem. **61**, 324 (1986); (c) A. Benmoussa, P. Labbé, D. Giroult, and B. Raveau, *ibid.* **44**, 318 (1982); (d) B. Domengès, F. Studer, and B. Raveau, Mat. Res. Bull. **18**, 669 (1983); (e) B. Domengès, M. Hervieu, B. Raveau, and R. J. D. Tilley, J. Solid State Chem. **54**, 10 (1984).

[2](a) J. P. Giroult, M. Goreaud, P. Labbé, and B. Raveau, J. Solid State Chem. **44**, 407 (1982); (b) A. Benmoussa, D. Giroult, P. Labbé, and B. Raveau, Acta Crystallogr. Sect. C **40**, 573 (1984); (c) B. Domengès, M. Goreaud, P. Labbé, and B. Raveau, J. Solid State Chem. **50**, 173 (1983); (d) M. Lamire, P. Labbé, M. Goreaud, and B. Raveau, *ibid.* **66**, 64 (1987); (e) A. Benmoussa, D. Giroult, and B. Raveau, Rev. Chim. Min. **21**, 710 (1984).

[3]M. Ghedira, H. Vincent, M. Marezio, J. Marcus, and G. Fourcadot, J. Solid State Chem. **56**, 66 (1985); L. Kihlborg, Arkiv Kemi **21**, 365 (1963); A. Magnéli, Acta Chem. Scand. **2**, 861 (1948).

[4]H. Guyot, C. Schlenker, G. Fourcadot, and K. Konaté, Solid State Commun. **54**, 909 (1985); M. Sato, K. Nakao, and S. Hoshino, J. Phys. C **17**, L817 (1984); C. Schlenker, S. S. P. Parkin, and H. Guyot, J. Magn. Magn. Mater. **54-57**, 1313 (1986); H. Guyot, C. Escribe-Filippini, G. Fourcadot, K. Konaté, and C. Schlenker, J. Phys. C **16**, L1227 (1983); H. Guyot, C. Schlenker, J. P. Pouget, R. Ayroles, C. Roucau, J. Phys. C **18**, 4427 (1985).

[5]E. Canadell, M.-H. Whangbo, C. Schlenker, and C. Escribe-Filippini, Inorg. Chem. **28**, 1466 (1989).

[6]E. Wang, M. Greenblatt, I. E.-I. Rachidi, E. Canadell, M.-H. Whangbo, and S. Vadlamannati, Phys. Rev. B **39**, 12 969 (1989).

[7](a) P. Monceau, in *Electronic Properties of Inorganic Quasi-One-Dimensional Compounds Part II,* edited by P. Monceau (Reidel, Dordrecht, The Netherlands, 1985), p. 139; (b) P. Haen, P. Monceau, B. Tissier, G. Waysand, A. Meerschaut, P. Molinié, and J. Rouxel, *Proceedings of the Fourteenth International Conference on Low Temperature Physics,* edited by M. Krusius and M. Vuorio (North-Holland, New York, 1975), Vol. 5, p. 445; E. Canadell, I. E.-I. Rachidi, J. P. Pouget, P. Gressier, A. Meerschaut, J. Rouxel, D. Jung, M. Evain, and M.-H. Whangbo, Inorg. Chem. **29**, 1401 (1990).

[8]E. Canadell, M.-H. Whangbo, and I. E.-I. Rachidi, Inorg.

Chem. **29**, 3871 (1990).
[9]M.-H. Whangbo and R. Hoffmann, J. Am. Chem. Soc. **100**, 6093 (1978).
[10]R. Hoffmann, J. Chem. Phys. **39**, 1397 (1963).
[11]M. Wolfsberg and L. Helmholtz, J. Chem. Phys. **20**, 837 (1952).
[12]E. Wang, M. Greenblatt, I. E.-I. Rachidi, E. Canadell and M.-H. Whanbgo, Inorg. Chem. **28**, 2451 (1989).
[13]J. H. Ammeter, H.-B. Bürgi, J. Thibeault, and R. Hoffmann, J. Am. Chem. Soc. **100**, 3686 (1978).
[14]P. Gressier, M.-H. Whangbo, A. Meerschaut, and J. Rouxel, Inorg. Chem. **23**, 1221 (1984); M.-H. Whangbo and P. Gressier, *ibid.* **23**, 1305 (1985); M.-H. Whangbo, F. J. DiSalvo, and R. M. Fleming, Phys. Rev. B **26**, 687 (1982); E. Canadell and M.-H. Whangbo, J. Am. Chem. **110**, 104 (1988).
[15](a) M.-H. Whangbo and L. F. Schneemeyer, Inorg. Chem. **25**, 2424 (1986); (b) M.-H. Whangbo, E. Canadell, and C. Schlenker, J. Am. Chem. Soc. **109**, 6308 (1987); (c) M.-H. Whangbo and E. Canadell, Acc. Chem. Res. **22**, 375 (1989).
[16]E. Canadell and M.-H. Whangbo, Chem. Rev. (to be published).
[17]M.-H. Whangbo, in *Electron Transfer in Biology and the Solid State: Inorganic Compounds with Unusual Properties,* edited by M. K. Johnson, R. B. King, D. M. Kurtz, Jr. C. Kutal, M. L. Norton, and R. A. Scott (American Chemical Society, Washington, D.C., 1990), p. 269.